IOP Publishing Phys. Med. Biol. 65 (2020) 015008 (17pp) https://doi.org/10.1088/1361-6560/ab491f

Physics in Medicine & Biology

IPEM Institute of Physics and Engineering in Medicine

PAPER

RECEIVED
24 June 2019

REVISED
24 September 2019

ACCEPTED FOR PUBLICATION
30 September 2019

PUBLISHED
10 January 2020

Modeling the radiation-induced cell death in a therapeutic proton beam using thermoluminescent detectors and radiation transport simulations

Alessio Parisi[1,3], Pawel Olko[2], Jan Swakoń[2], Tomasz Horwacik[2], Hubert Jabłoński[2], Leszek Malinowski[2], Tomasz Nowak[2], Lara Struelens[1] and Filip Vanhavere[1]

[1] Belgian Nuclear Research Centre SCK·CEN, Mol, Belgium
[2] Institute of Nuclear Physics, Polish Academy of Sciences (IFJ PAN), Krakow, Poland
[3] Author to whom correspondence should be addressed.

E-mail: alessio.parisi@sckcen.be

Keywords: proton therapy, thermoluminescent detectors, Microdosimetric d(z) model, RBE, modified MKM, PHITS

Abstract

Changes in the relative biological effectiveness (RBE) of the radiation-induced cell killing of human salivary glands (HSG) were assessed along the Bragg peak of a 60 MeV clinical proton beam by means of coupling biophysical models with the results of Monte Carlo radiation transport simulations and experimental measurements with luminescent detectors. The fluence- and dose-mean unrestricted proton LET were determined along the Bragg peak using a recently developed methodology based on the combination of the response of ^{7}LiF:Mg,Ti (MTS-7) and ^{7}LiF:Mg,Cu,P (MCP-7) thermoluminescent detectors. The experimentally assessed LET values were compared with the results of radiation transport simulations using the Monte Carlo code PHITS, showing a good agreement. The cell survival probabilities and RBE were then calculated using the linear-quadratic model with the linear term derived using a phenomenological LET-based model (Carabe A *et al* 2012 *Phys. Med. Biol.* **57** 1159) in combination with the experimentally-assessed or PHITS-simulated dose mean proton LET values. To the same aim, PHITS simulated microdosimetric spectra were used as input to the modified microdosimetric kinetic model (modified MKM, (Kase *et al* 2006 *Radiat. Res.* **166** 629–38)). The RBE values calculated with the three aforementioned approaches were compared and found to be in very good agreement between each other, proving that by using dedicated pairs of thermoluminescent detectors it is possible to determine ionization density quantities of therapeutic proton beams which can be applied to predict the local value of the RBE.

Abbreviations used in the paper

CHO	Chinese hamster ovary
FWHM	Full width at half maximum
HSG	Human salivary gland
LEM	Local effect model
LET	Linear energy transfer
MKM	Microdosimetric kinetic model
PMMA	Polymethyl methacrylate
RBE	Relative biological effectiveness
SOBP	Spread out Bragg peak
TEPC	Tissue equivalent proportional counter
TLD	Thermoluminescent detector
TPS	Treatment planning system

1. Introduction

Dose prescription in proton radiotherapy is currently performed by upscaling the physical absorbed dose by 10% in respect to conventional MV x-ray therapy (International Commission on Radiation Units and Measurements 2007, International Atomic Energy Agency 2008), thus considering protons being 1.1 times more effective than photons for tumor control purposes regardless of the treated tissue, the heterogeneous radiosensitivity of the cells composing the human body, the dose fractionation scheme and possible changes in the effectiveness of the treatment within the irradiated volume.

This relative biological effectiveness (RBE) value of 1.1 for protons was deduced by averaging the results of *in vivo* studies performed in the middle of different proton spread out Bragg peaks (SOBPs) over all dose levels (Paganetti *et al* 2002). The RBE values ranged from 0.7 to 1.6 with a moderate but statistically relevant increase at lower dose levels. At the same time, the results of *in vitro* colony formation cell survival experiments were found to be more scattered, ranging from 0.9 to 2.1 around an average RBE value of approximately 1.2 (Paganetti *et al* 2002). In this case, a more pronounced RBE increase at lower proton doses was observed in respect to the *in vivo* studies. Furthermore, the experiments indicated a clear RBE rise in the final part of the Bragg peak, where protons are close to their stop in matter. Here, relevant changes in the pattern of energy deposition are occurring due to the higher proton linear energy transfer (LET) and the creation of strongly ionizing secondary fragments (Paganetti 2002, Durante and Paganetti 2016). All of this may translate in a possible underestimation of the biological range of the treatment, a consequent unwanted exposure of an organ at risk and a higher risk of secondary cancer development (Wilkens and Oelfke 2004, Carabe *et al* 2012). Nevertheless, it was concluded that, because of the big uncertainties associated with the assessed proton RBE values, the use of a generic value of 1.1 in respect to photons can be judged appropriate in clinical practice and the treatment plans optimized based on physical dose only (Paganetti *et al* 2002).

On the other hand, more recent studies highlighted the need for considering possible inhomogeneities in the treatment effectiveness, especially in the distal part of the irradiated volume, and the strong dependence of the proton RBE on the considered biological endpoint, the cell radiosensitivity and the proton absorbed dose level (Kase *et al* 2013, Chaudhary *et al* 2014, Paganetti 2014, Giovannini *et al* 2016, Debrot *et al* 2018). As an immediate consequence, a large and growing body of literature investigated the possibility of including RBE weighted doses in the planning of proton therapy treatments with the primary aim of preventing possible RBE hotspots (Tilly *et al* 2005, Frese *et al* 2011, Buchsbaum *et al* 2014, Unkelbach *et al* 2016, Wan Chan Tseung *et al* 2016, McMahon *et al* 2018). To this aim, models correlating biophysical endpoints to physical quantities such as the linear energy transfer (Belli *et al* 1997, Wilkens and Oelfke 2004, Chen and Ahmad 2011, Carabe *et al* 2012, Wedenberg *et al* 2013, Jones 2015, McNamara *et al* 2015, Mairani *et al* 2017, Rørvik *et al* 2017) or the microdosimetric lineal energy (Loncol *et al* 1994, Hawkins 1996, 2003, Kase *et al* 2006, Sato and Furusawa 2012) were developed, validated against experimental biological data and employed in the aforementioned calculations. The determination of the LET and the lineal energy probability density needed for the RBE assessment is generally performed by employing radiation transport computer simulations (Grassberger and Paganetti 2011, Guan *et al* 2015, Takada *et al* 2017) or active, complex microdosimetric detectors (Kase *et al* 2013, Rosenfeld 2016, Colautti *et al* 2018). An alternative methodology to assess average LET values for in-phantom measurements in proton therapy using passive, cheap, safe thermoluminescent detectors (TLDs) was developed and preliminarily validated by exposing the detectors in a clinical proton spread out Bragg peak (SOBP, range ~ 120 mm, modulation ~ 50 mm, max energy ~ 200 MeV) at iThemba LABS (Parisi *et al* 2019a). The LET values determined using thermoluminescent detectors agreed well with the results of radiation transport simulations using Geant4. Additionally, using the experimentally assessed dose mean LET values as input for the LET-vs-RBE model of Paganetti (2014), the RBE was calculated at different depths within the proton SOBP for Chinese Hamster Ovary (CHO) cells and compared with the results of an *in vitro* colony survival study, showing a good agreement (Parisi *et al* 2019a).

In this work, we investigate the RBE changes within a pristine proton Bragg peak (range ~ 30 mm, max energy ~ 60 MeV) at the eye treatment beamline of the proton therapy facility Cyclotron Center Bronowice by coupling the results of experimental measurements using thermoluminescent detectors, Monte Carlo computer simulations and two different biophysical cell-survival models.

Firstly, using an improved version of the method described in Parisi *et al* (2019a), the response of two types of detectors was combined to calculate the fluence- and dose-mean unrestricted LET in water as function of the depth in water and compared to the results of the Monte Carlo radiation transport simulations with the PHITS code (Sato *et al* 2018). Thus, using the experimentally determined and PHITS-simulated dose-mean LET values as input for the biophysical model of Carabe *et al* (2012), the survival curves for human salivary gland (HSG) cells were predicted as function of the depth in water. Afterwards, the survival fraction and the RBE in case clinical proton doses of 2 and 6 Gy were assessed for both cases (experimentally or simulated LET values as input for the calculations). It worth underling that this paper represents the first time that cell survival probabilities are assessed by means of coupling experimental measurements with thermoluminescent detectors and a biophysical

LET-based model. Finally, in order to further validate and benchmark the obtained results, a comparison was performed with an independent approach employing the modified microdosimetric kinetic model (modified MKM, Kase *et al* 2006) in combination with PHITS-simulated lineal energy probability density along the proton Bragg peak for the cell line and proton doses of hereinabove.

2. Methodology

2.1. Thermoluminescent detectors

Two types of thermoluminescent detectors were used in this work: ^{7}LiF:Mg,Ti (MTS-7) and ^{7}LiF:Mg,Cu,P (MCP-7) detectors produced by the Institute of Nuclear Physics, Polish Academy of Sciences (IFJ PAN) in Krakow, Poland (Bilski 2002). The detectors have the form of a cylindrical pellet with a diameter of 4.5 mm and a thickness of 0.9 mm. Detectors made of ^{7}LiF were used in order to reduce their sensitivity to the neutrons produced as secondary radiation in proton therapy. Two packages of background detectors were used to assess and afterwards subtract the background dose accumulated during transportation and storage of the experimental and calibration detectors. Three detectors of each type were used for each measurement position within the proton Bragg peak and for the background packages.

2.1.1. Thermal treatments

Before the experimental irradiations, the detectors were annealed in temperature controlled ovens according to the standard protocols (McKeever *et al* 1995): 1 h at 400 °C followed by 2 h at 100 °C for ^{7}LiF:Mg,Ti (MTS-7) detectors or 10 min at 240 °C for ^{7}LiF:Mg,Cu,P (MCP-7) detectors. Afterwards, the detectors were allowed to cool down in air at room temperature (^{7}LiF:Mg,Ti detectors) or at -10 °C inside a freezer (^{7}LiF:Mg,Cu,P detectors). In order to prevent the occurrence of low temperature anomalies in the glow curve structure of LiF:Mg,Cu,P detectors (Parisi *et al* 2018a) and to minimize fading effects, a post-irradiation pre-readout protocol of 30 min at 120 °C was applied to all detectors. Afterwards, the detectors were removed from the temperature controlled oven and allowed to cool down in air at room temperature.

2.1.2. Readout

The acquisition of the radiation-induced light signal was performed using an automatic Harshaw 5500 reading system manufactured by Thermo Fisher Scientific. The detectors were heated by a flux of hot nitrogen from room temperature up to a maximum temperature of 340 °C (LiF:Mg,Ti detectors) or 240 °C (LiF:Mg,Cu,P detectors) with a constant heating rate of 1 °C s^{-1}. The background packages and the calibration detectors were read together with the experimental ones to minimize fading effects or possible changes in the sensitivity of the reader system. In addition, the stability of the latter is monitored on a daily basis by reading ^{nat}LiF:Mg,Cu,P (MCP-N) detectors exposed to a known γ-ray dose.

2.1.3. Luminescent signal quantification

Because of the strong influence of the glow curve signal quantification method on the dose assessment process (Parisi *et al* 2017a), the glow curves were individually processed in terms of inherent background subtraction, smoothing, normalization and count integration. The subtraction of the LiF:Mg,Ti inherent background signal was handled accordingly to the methodology described in Parisi *et al* (2017b). Afterwards, the glow curves were imported in the GlowView software version 1.3 (Gieszczyk and Bilski 2017). The position of the main peak of the glow curves was normalized to 220 °C in case of LiF:Mg,Ti detectors and to 210 °C for LiF:Mg,Cu,P detectors. The luminescent signal was quantified by a count integration over the following temperature ranges: 150 °C–248 °C (LiF:Mg,Ti detectors) or 150 °C–240 °C (LiF:Mg,Cu,P detectors).

2.1.4. Calibration

The calibration of the detectors was achieved by irradiating seven detectors of each type with 0.5 Gy air kerma from a ^{60}Co γ-ray source at the secondary standard calibration laboratory of the Belgian Nuclear Research Centre SCK·CEN. The air kerma values were converted to absorbed dose in water using a value of 1.11 derived from the ratio of the mass absorption coefficients of air and water for ^{60}Co γ-rays in case of electronic equilibrium. The latter was achieved by placing a 4 mm polymethyl methacrylate (PMMA) build up layer between the source and the detectors. The values of the mass absorption coefficients for air and water were extracted from the mass attenuation and mass energy absorption tables of the National Institute of Standards and Technology (NIST, Maryland, United States of America, http://physics.nist.gov/xaamdi).

2.1.5. Individual sensitivity correction

In order to decrease the sensitivity spread among the different detectors, individual sensitivity factors were determined after the experimental campaign by irradiating the detectors with 50 mGy air kerma from a

calibrated ^{60}Co γ-ray source at the secondary standard calibration laboratory of the Belgian Nuclear Research Centre SCK·CEN. All operational protocols (annealing, pre-heat, readout and data processing) used for the determination of the individual sensitivity factors were the same as the ones used for the experimental, calibration and background detectors. Each individual sensitivity factor was calculated as the ratio between the quantified light signal for a specific detector over the same quantity averaged over all detectors of the same type.

2.1.6. Dose assessment

The absorbed dose in water measured by a detector exposed to protons ($D_{\text{water, exp}}$) was calculated using equation (1), where S is the luminescent signal of the detector under analysis, $\overline{S}_{\text{BG exp}}$ is the average luminescent signal of the background detectors transported to Poland, $\overline{S}_{\text{cal}}$ is the average luminescent signal of the calibration detectors irradiated with 0.5 Gy air kerma ($k_{\text{air, cal}}$) from the ^{60}Co γ-ray source, $\overline{S}_{\text{BG cal}}$ is the average luminescent signal of the detectors used to assess the background dose of the calibration detectors and 1.11 is the conversion factor between air kerma and dose in water for ^{60}Co γ-ray exposures.

$$D_{\text{water, exp}} = 1.11 \frac{S - \overline{S}_{\text{BG exp}}}{\left(\overline{S}_{\text{cal}} - \overline{S}_{\text{BG cal}}\right)} k_{\text{air, cal}} \quad (1)$$

2.2. Proton irradiations

All the proton irradiations included in this work were performed in the cancer therapy room of the Centrum Cyklotronowe Bronowice (CCB) of the Institute of Nuclear Physics, Polish Academy of Sciences (IFJ PAN), Krakow (Poland). The 60 MeV proton beam is extracted from the AIC-144 isochronous cyclotron, initially built for physics research and afterwards adapted to medical applications (Bakewicz *et al* 2003, Swakon *et al* 2010), and transported to the therapy room through a 25 m beam transport system including bending, quadrupole and correction magnets, a tantalum scatterer, beam monitors, range shifter and modulators. More details can be found in Swakon *et al* (2010). The 60 MeV collimated proton beam is perfectly suited for this type of studies due to the very high (~5) peak to plateau ratio for the Bragg peak in water. The proton beam reference dosimetry was performed according to International Atomic Energy Agency, 2000 using a PTW 23342 Markus ionization chamber moved in a water phantom by a 3D scanner with a spatial resolution better than 0.1 mm. The uncertainty in the delivered proton dose was assessed being 2%.

As shown in figure 1, the thermoluminescent detectors were placed inside a PMMA phantom and hold in position by a thin kapton foil in front of the detectors. Measurements at nine positions (equivalent depth in water of the front surface of the detector ~ 0, 3.7, 8.3, 14.2, 18.8, 23.4, 25.9, 27.1, 28.2 mm) within a pristine Bragg peak (range in water ~ 30 mm) were achieved by placing PMMA plates of different thicknesses upstream from the detectors. The PMMA plates were tightly hold by using a spring and the surface of the inner PMMA plate was levelled with the one of the kapton foil. The nine measurement positions are summarized in figure 2 together with the relative absorbed dose profile measured with the Markus ionization chamber. The points represent the central point of the thermoluminescent detectors, while the horizontal error bars include both the water equivalent thickness of the detectors and the uncertainty of the positioning system (±0.1 mm, Swakon *et al* 2010).

The water equivalent thickness of the detectors was calculated as the average ratio of the range in water and lithium fluoride assessed using the Stopping and Range of Ions in Matter (SRIM) software suite version 2013.00 (Ziegler *et al* 2010), being 1.8 mm for a 0.9 mm thick lithium fluoride detector with density of 2.5 g cm^{-3}. In a similar way, the water equivalent diameter of the detector was assessed being 9 mm. The water equivalent depths of the applied PMMA plates were determined by measurements of depth dose profiles using the Markus ionization chamber in a dedicated 10 × 10 × 10 cm^3 water phantom.

2.3. Monte Carlo radiation transport simulations of the proton Bragg peak

2.3.1. PHITS

All the radiation transport simulations included in this work were carried out using the Monte Carlo Particle and Heavy Ion Transport code System (PHITS) version 3.09 (Sato *et al* 2018). The simulation cutoff was set to 1 keV u^{-1} for all particles (ions, electrons, positrons, photons, muons, mesons, baryons, neutrinos…), with the only exception of neutrons for which a value of 10^{-10} MeV was chosen. The energy loss of charged particles, with the exception of photons, electrons and positrons, was assessed with the stopping power calculation model ATIMA (http://web-docs.gsi.de/~weick/atima) under the continuous slowing down approximation (CSDA). On the other hand, the Electron Gamma Shower version 5 (EGS5) code (Hirayama *et al* 2005) was employed to simulate the transport of photons, electrons and positrons. The energy straggling of charged particles was considered by means of the Landau Vavilov formula (Vavilov 1957). The angular straggling was taken into account through the use of the Lynch's Coulomb diffusion formula (Lynch and Dahl 1991) based on Moliere theory (Moliere

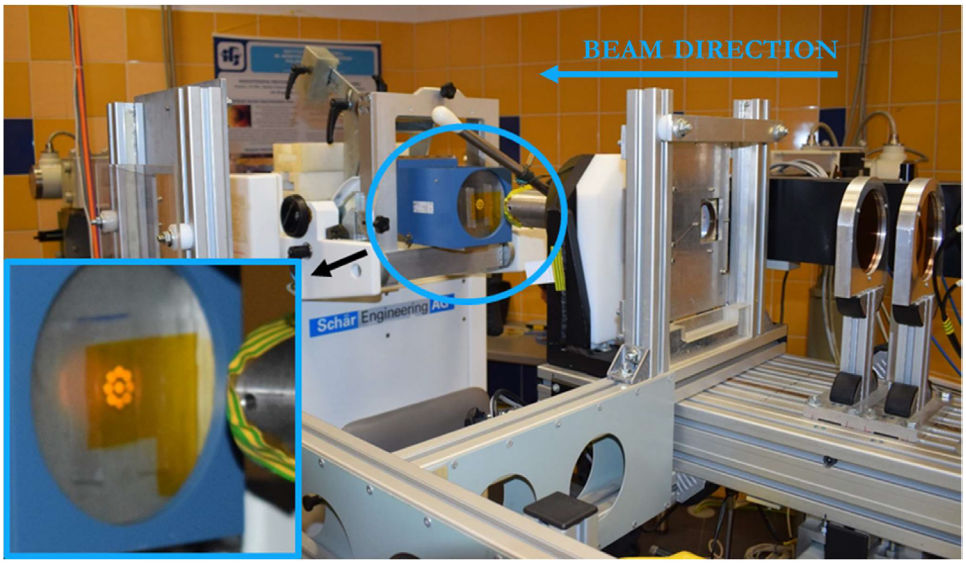

Figure 1. Picture of the irradiation setup including a detailed view on the thermoluminescent detectors.

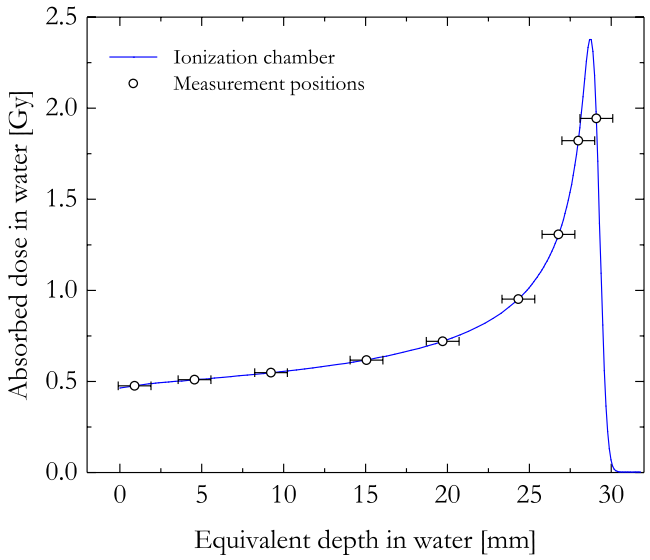

Figure 2. Measurement positions of the thermoluminescent detectors along the proton Bragg peak. The blue line represents the absorbed dose profile measured with the ionization chamber. The points indicate the water equivalent depth of the center of the detectors, while the horizontal error bars include both the water equivalent thickness of the detectors and the uncertainty of the positioning system.

1948). Hadrons and nucleus induced nuclear reactions were simulated using the intra-nuclear cascade models JAM and INCL and the quantum molecular dynamics model JQMD (Sato *et al* 2018). The evaporation and fission model GEM was adopted for simulating the static stage after both hadron and nucleus induced nuclear reactions (Sato *et al* 2015). The Event Generator Mode (EGM) version 2 (Ogawa *et al* 2014) was used to handle the transport and the interactions of low energy neutrons. The assessment of the single event microdosimetric specific energy probability density needed for the calculation of the relative efficiency of both types of detectors with the Microdosimetric d(z) Model (Parisi *et al* 2018b) and the lineal energy probability density needed for the cell survival modeling using the modified microdosimetric kinetic model (modified MKM, Kase *et al* 2006) was performed by employing the microdosimetric function (Sato *et al* 2006, 2012) implemented in the PHITS code.

2.3.2. Simulation of the depth dose profile

The initial energy distribution of the protons was supposed to be Gaussian shaped. In order to precisely determine the center and full width at half maximum (FWHM) of the proton energy distribution, the absorbed dose profile measured by the ionization chamber was compared with simulated Bragg peaks and varying the two former parameters. To this aim, several hundreds of center energy-FWHM combinations were tested. Using

the [T-Deposit] tally of PHITS, the energy deposition was scored in a water phantom ($\rho = 1\,\mathrm{g\,cm^{-3}}$) in 0.2 mm cylindrical steps with bases perpendicular to the beam direction. 10^8 particles were simulated for each run in order to achieve a statistical uncertainty of all simulated parameters well below 0.1%.

2.3.3. LET assessment within the pristine Bragg peak

The LET in water was evaluated in the same cylindrical computational domains of section 2.3.2, using the PHITS [T-LET] tally. In the latter case, the fluence and dose distributions of the proton LET were assessed as function of the LET in a logarithmic binning from 0.01 to 10 000 keV $\mu\mathrm{m}^{-1}$ with 50 bins per decade. Finally, the unrestricted proton fluence- and dose-mean LET values were calculated using equations (2) and (3), where $\Phi(\mathrm{LET})$ and $d(\mathrm{LET})$ represent the proton fluence- and dose-probability density of the LET as function of the LET.

$$\overline{\mathrm{LET}}_{\mathrm{F}} = \int_0^{+\infty} \mathrm{LET}\ \Phi(\mathrm{LET})\ d\mathrm{LET} \tag{2}$$

$$\overline{\mathrm{LET}}_{\mathrm{D}} = \int_0^{+\infty} \mathrm{LET}\ d(\mathrm{LET})\ d\mathrm{LET} \tag{3}$$

2.3.4. Lineal energy assessment within the pristine Bragg peak

The lineal energy (y, International Commission on Radiation Units and Measurements 1983) in water was calculated in the aforementioned cylindrical computational domains by using the PHITS [T-SED] tally based on the microdosimetric function implemented in PHITS. The frequency- and dose-distributions of the lineal energy were scored in a spherical site of diameter equal to 0.564 μm as needed for calculations performed using the modified MKM in case of human salivary gland (HSG) cells (Sato *et al* 2011). A logarithmic binning from 0.001 to 10 000 keV $\mu\mathrm{m}^{-1}$ with 50 bins per decade was used. The minimum energy deposition considered in this study for the assessment of microdosimetric probability density was the one related to an event characterized by one ionization only. The frequency- and dose-mean expectation values of the lineal energy (respectively $\bar{y}_{\mathrm{F}}$ and $\bar{y}_{\mathrm{D}}$) were determined as in equations (4) and (5), where $f(y)$ and $d(y)$ represent the frequency- and dose-probability density of the lineal energy as function of the lineal energy.

$$\bar{y}_{\mathrm{F}} = \int_0^{+\infty} y\, f(y)\ dy \tag{4}$$

$$\bar{y}_{\mathrm{D}} = \int_0^{+\infty} y\, d(y)\ dy \tag{5}$$

Additionally, the saturation corrected lineal energy $y*$ (International Commission on Radiation Units and Measurements 1983) was calculated using equation (6) for a saturation parameter y_0 of 93.4 keV $\mu\mathrm{m}^{-1}$, assessed by Sato *et al* (2011) as the optimal one for human salivary gland (HSG) cells.

$$y^* = \frac{y_0^2 \int_0^{+\infty} \left[1 - \exp\left(-\frac{y}{y_0}\right)\right] f(y)\ dy}{\int y\, f(y)\ dy} \tag{6}$$

2.4. The Microdosimetric d(z) Model

The relative efficiency of luminescent detectors depends strongly on both the particle type to be measured and its LET, with very low efficiency values at high LET. This efficiency decrease at high LET is due to a local saturation of the luminescent centers because of the very dense pattern of energy deposition. However, this efficiency decrease is not an unique function of the LET, being different the microscopic pattern of energy deposition of two different particles (i.e. protons and alpha particles) with the same LET. The Microdosimetric d(z) Model (Parisi 2018, Parisi *et al* 2018b) is a recently developed model able to describe and predict the relative luminescence efficiency of luminescent detectors exposed to different radiation qualities in both homogenous and mixed fields (multi-energy and multi-particle fields) by analyzing their stochastic energy deposition at the nanoscale. The relative luminescence efficiency (η_{rel}) is defined as in equation (7) as the ratio between the intensity of the luminescence signal S per unit of absorbed dose D for the radiation under investigation over the same quantity for a reference radiation.

$$\eta_{\mathrm{rel}} = \frac{\left(S/D\right)_{\mathrm{radiation}}}{\left(S/D\right)_{\mathrm{reference\ radiation}}} \tag{7}$$

As in Olko's microdosimetric model (Olko 2002, 2004), it is assumed that a luminescent detector is being composed by many independent structures, called targets, which act as sensitive volumes for measuring

radiation. The key idea of the Microdosimetric d(z) Model is that the relative efficiency of luminescent detectors can be correlated with the microscopic pattern of energy deposition in nanometric targets quantified by means of the microdosimetric specific energy dose-probability density (International Commission on Radiation Units and Measurements 1983). The dimension of these radiation sensitive structures is not known *a priori* and represents the free parameter of the model.

According to the formalism of the Microdosimetric d(z) Model, the relative efficiency of luminescent detectors can be calculated using equation (8) where $d(z)$ is the dose probability density of the specific energy z and $r(z)$ is a specific energy response function uniquely defined for each detector type. The reference radiation was chosen to be the photons from a ^{60}Co γ-ray source. The slowing down of the particle beam within the 0.9 mm detector thickness and the creation of secondary particles were taken into account in the simulations. More details on the Microdosimetric d(z) Model and on the assessment of $d(z)$ and $r(z)$ can be found in Parisi (2018) and Parisi *et al* (2018b).

$$\eta_{\text{rel}} = \frac{\left[\int_0^{+\infty} d(z)\ r(z)\ dz\right]_{\text{radiation}}}{\left[\int_0^{+\infty} d(z)\ r(z)\ dz\right]_{\text{reference radiation}}} \tag{8}$$

Under these assumptions, the model was benchmarked for LiF:Mg,Ti (MTS) and LiF:Mg,Cu,P (MCP) thermoluminescent detectors through a comparison with experimentally determined efficiency data in case of charged particles from ^{1}H to ^{132}Xe (simulated energy range: 3–1000 MeV u^{-1}) and photons (simulated energy range = 10–1250 keV). A very good agreement was found for the whole particle and energy ranges in case of model calculations performed in a site size of 40 nm using the Monte Carlo code PHITS (Parisi *et al* 2017c, 2017d, 2018b, 2019b, Parisi 2018).

In order to confirm the minor effect of the detectors' dopants in the aforementioned calculations, all simulations of this work were performed in both pure lithium fluoride (no dopants) and lithium fluoride including also the nominal dopant concentrations of the two detector types. As in Parisi *et al* (2018b), the presence of the dopants was found to play a negligible role in the assessment of all the physical quantities, with an average deviation smaller than 0.1%. Consequently, the discussion is limited to calculations performed in lithium fluoride.

2.5. LET assessment with thermoluminescent detectors

The experimental assessment of the proton LET was performed by means of a recently developed methodology based on the different relative efficiency of ^{7}LiF:Mg,Ti (MTS-7) and ^{7}LiF:Mg,Cu,P (MCP-7) detectors for measuring charged particles (Parisi *et al* 2019a). A simulated ^{7}lithium fluoride cylinder representative of our detectors (density = 2.5 g cm^{-3}, diameter = 4.5 mm, thickness = 0.9 mm) was irradiated with monoenergetic proton beams (diameter = 9 mm) and the dose probability density of the specific energy was assessed for the optimal site size of 40 nm. The relative efficiency (η_{rel}) of the two detector types was then calculated using the Microdosimetric d(z) Model (section 2.4) and the ratio between their predicted response was determined. At the same time, the unrestricted proton $\overline{\text{LET}}_{\text{F}}$ and $\overline{\text{LET}}_{\text{D}}$ averaged over the detector volume were assessed with PHITS the [T-LET] tally for each proton energy and correlated with the aforementioned ratio. A constant factor of 2.0 was used to convert LET in lithium fluoride to LET in water. Thus, knowing the ratio between the absorbed doses measured by ^{7}LiF:Mg,Ti (MTS-7) and ^{7}LiF:Mg,Cu,P (MCP-7) detectors, the unrestricted proton $\overline{\text{LET}}_{\text{F}}$ and $\overline{\text{LET}}_{\text{D}}$ in water can be calculated. In order to improve the goodness of the correlation between the aforementioned ratio and the proton LET quantities, the simulations of Parisi *et al* (2019a) (performed using PHITS 2.82) were repeated using PHITS 3.09 for all the proton energies of our previous work (3, 5, 7, 10, 15, 20, 30, 40, 50, 60, 70, 80, 90, 100, 125, 150 and 250 MeV) and including more energy points (2, 4, 6, 8, 9, 11, 12, 12.5, 12.6, 12.75, 13, 13.5, 14, 17, 500, 1000 MeV).

2.6. Cell death modeling

According to the linear quadratic model (McMahon 2019), the survival probability of a cell exposed to a single dose of radiation (D) can be expressed as in equation (9), where α and β are, respectively, the linear and quadratic parameters describing the radiosensitivity of the cell.

$$\text{Survival probability} = e^{(-\alpha D - \beta D^2)}. \tag{9}$$

While a mechanistic interpretation of the latter parameters was topic of discussions for years, it is generally accepted that α represents the contribution of lethal damages occurring from single particle hits, while β takes into account the cell inactivation due to the interaction of multiple sublethal events. In this work, two different approaches were employed for modeling α and β: the LET based model of Carabe *et al* (2012) and the modified microdosimetric kinetic model (modified MKM) of Kase *et al* (2006). In both cases, the cell line under investigation was chosen to be the human salivary glands (HSG). The aforementioned tumor cell line was chosen

because of its common use for preclinical studies and treatment planning with protons and carbon ions (Inaniwa *et al* 2010, Kase *et al* 2011, 2013, Inaniwa and Kanematsu 2018).

Once the linear and quadratic terms are known for both the radiation quality under study (α and $ß$) and a reference radiation (α_{ref} and $ß_{ref}$), the RBE can be assessed as function of the dose D of the radiation under investigation using equation (10) (Wilkens and Oelfke 2004, Chen and Ahmad 2011, Paganetti *et al* 2019).

$$\mathrm{RBE} = \frac{\sqrt{\alpha^2_{\mathrm{ref}} + 4\,\beta_{\mathrm{ref}}\,D\,(\alpha + \beta\,D)} - \alpha_{\mathrm{ref}}}{2\,\beta_{\mathrm{ref}}\,D}. \tag{10}$$

The α_{ref} and $ß_{ref}$ values for HSG cells in case of photon exposure were extracted from Furusawa *et al* (2000) being, respectively, 0.313 Gy^{-1} and 0.0615 Gy^{-2}. In this work, the RBE was calculated in case of clinically relevant proton doses of 2 and 6 Gy (Paganetti 2014).

2.6.1. Phenomenological LET based model

A literature study was performed in order to choose which phenomenological $\overline{\mathrm{LET}}_{\mathrm{D}}$ model to be used in this study. At first, the models not accounting for the different radiosensitivity of the cell line under investigation (usually quantified by means of the ratio between the α_{ref} and $ß_{ref}$ terms of the linear quadratic model) were excluded (Belli *et al* 1997, Wilkens and Oelfke 2004, Chen and Ahmad 2011). Secondly, the Jones (2015) model was discarded due to the significantly higher calculated RBE values in comparison to other models, as shown for instance in Rørvik *et al* (2018). Finally, due to its simplicity, the widespread utilization and the use of absolute proton $\overline{\mathrm{LET}}_{\mathrm{D}}$ values, the model of Carabe *et al* (2012) was preferred to the McNamara *et al* (2015), Mairani *et al* (2017) and Rørvik *et al* (2017) ones which employ rescaled proton LET quantities.

The Carabe *et al* (2012) model is based on the assumption that, in case of proton exposures, α linearly correlates with α_{ref} with a slope depending on both the unrestricted proton $\overline{\mathrm{LET}}_{\mathrm{D}}$ in water and the ($\alpha_{ref}/ß_{ref}$) ratio, as in equation (11).

$$\alpha = 0.843 + 0.414\frac{\overline{\mathrm{LET}}_{\mathrm{D}}}{\left(\alpha_{\mathrm{ref}}/\beta_{\mathrm{ref}}\right)}. \tag{11}$$

On the other hand, for consistency with the modified microdosimetric kinetic model (see section 2.6.2), the $ß$ term of the linear quadratic model was considered to be independent from the radiation quality and equal to the one obtained after photon irradiation $ß_{ref}$.

2.6.2. Modified microdosimetric kinetic model

The microdosimetric kinetic model (MKM, Hawkins 1996, 2003) was modified by Kase *et al* (2006) in order to account for the cell overkilling effect by introducing in its formalism the concept of saturation corrected lineal energy (equation (6), International Commission on Radiation Units and Measurements 1983). The radiation induced cell killing is assumed to be related to the specific energy probability density in sub-nuclear regions of the cell called domains. To this aim, the α term of the linear quadratic model can be assessed using equation (12), where α_0 represents the initial slope of the survival curve in the limit of $LET \to 0$, $ß_{ref}$ is the quadratic term of the linear quadratic model in case of the reference photon exposure and $\bar{z}^*_{1D,\,d}$ is the single-event dose-mean saturation-corrected specific energy in the domain.

$$\alpha = \alpha_0 + \beta_{\mathrm{ref}}\,\bar{z}^*_{1D,\,d}. \tag{12}$$

The latter quantity can be obtained as in equation (13) where l_d, m_d, y^*_d, ρ_d and r_d are, respectively, the mean chord length, the mass, the saturation corrected lineal energy, the density (=1.0 g cm^{-3}) and the radius of the domain.

$$\bar{z}^*_{1D,\,d} = \frac{l_d}{m_d}\,y^*_d = \frac{1}{\rho_d\,\pi\,r_d^2}\,\frac{y_0^2\int_0^{+\infty}\left[1-\exp\left(-\frac{y}{y_0}\right)\right]f(y)\,dy}{\int y\,f(y)\,dy}. \tag{13}$$

The numeric value of the saturation parameter y_0 can be calculated according to equation (14), where R_n is the radius of the nucleus of the target cell.

$$y_0 = \frac{\rho_d\,\pi\,r_d\,R^2_n}{\sqrt{\beta_{\mathrm{ref}}(r^2_d + R^2_n)}}. \tag{14}$$

The determination of the free parameters of the modified MKM is not straightforward and usually achieved by fitting the model results to experimental data. In this work, we used the numerical values of the modified MKM parameters for HSG cells as previously determined by Sato *et al* (2011), namely $\alpha_0 = 0.155\ Gy^{-1}$, $r_d = 0.282\ \mu m$, $R_n = 4.19\ \mu m$ and $y_0 = 93.4\ keV\ \mu m^{-1}$. The $ß$ term of the linear quadratic model is assumed be equal to $ß_{ref}$ independently from the radiation quality (Kase *et al* 2006).

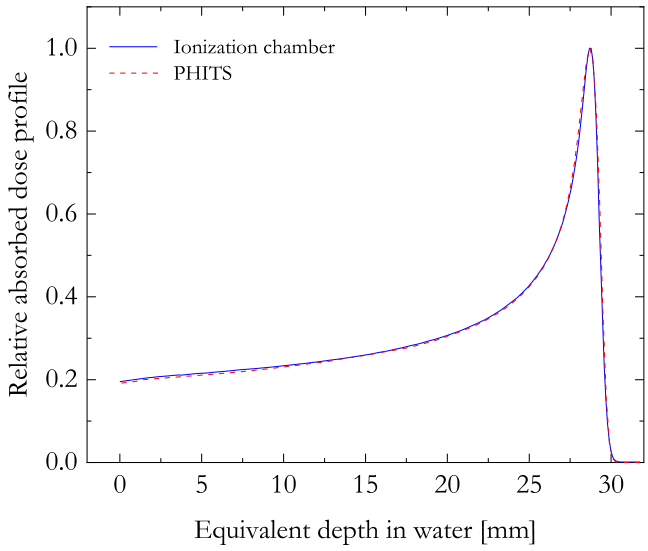

Figure 3. Comparison between the relative depth dose profiles measured with the ionization chamber and simulated using PHITS.

3. Results

3.1. Monte Carlo simulations of the proton Bragg peak

3.1.1. Depth dose profile

The best agreement between the PHITS simulated depth dose profile and the results of the measurements performed using the Markus ionization chamber was obtained in case of calculations performed with an asymmetric Gaussian distribution of the proton energy source centered at 58.4 MeV, with a FWHM of 1.4 MeV and an upper Gaussian energy cutoff of 58.55 MeV. The two relative absorbed depth dose profiles, normalized to their maximum, are plotted in figure 3 as function of the depth in water. The ratio between the dose at maximum and dose at the entrance plateau was calculated being 5.2 with a distal falloff (defined as the distance between 90% and 10% of the dose at maximum) of approximately 0.8 mm. The average relative deviation between the two curves was found to be smaller than the uncertainty in the delivered proton dose (2%).

3.1.2. Linear energy transfer

Using, respectively, equations (2) and (3), the fluence- and dose-mean values of the unrestricted proton LET in water were calculated from the LET probability density simulated using PHITS. The results are plotted in figure 4 as function of the depth in water. Here and in other figures, the relative absorbed dose profile measured by the ionization chamber is given as a reference for the position along the Bragg peak. As the transported beam was not monoenergetic, the $\overline{\mathrm{LET}}_{\mathrm{D}}$ values were always higher than the $\overline{\mathrm{LET}}_{\mathrm{F}}$ ones ranging from approximately 1 keV μm^{-1} at the entrance plateau up to roughly 22 keV μm^{-1} ($\overline{\mathrm{LET}}_{\mathrm{F}}$) or 31 keV μm^{-1} ($\overline{\mathrm{LET}}_{\mathrm{D}}$) at the end of the proton path in water.

3.1.3. Lineal energy

In a similar way, using the PHITS-simulated frequency- and dose-probability density of the lineal energy in water for a 0.564 μm site, the frequency- and dose-mean lineal energy (respectively $\bar{y}_{\mathrm{F}}$ and $\bar{y}_{\mathrm{D}}$) were calculated according equations (4) and (5) and plotted in figure 5 as function of the depth in water. In addition, also the saturation corrected lineal energy $y*$ (equation (6), saturation parameter $y_0 = 93.4$ keV μm^{-1}) was included for comparison in figure 5. The three quantities were found to show no significant changes between the entrance plateau until a depth in water of approximately 20 mm around an average value of roughly 0.9, 4.8, 2.8 keV μm^{-1} for $\bar{y}_{\mathrm{F}}$, $\bar{y}_{\mathrm{D}}$ and $y*$, respectively. A sharp increase of the latter three quantities is observed for depth in water above 27 mm up to a maximum value of 12, 30 and 26 keV μm^{-1}, respectively.

3.2. LET assessment with thermoluminescent detectors

3.2.1. Calibration curves

Figure 6 correlates the average unrestricted proton LET quantities the expected ratio between the absorbed dose measured by ^{7}LiF:Mg,Ti (MTS-7) and ^{7}LiF:Mg,Cu,P (MCP-7) thermoluminescent detectors as predicted using the Microdosimetric d(z) Model in combination with the Monte Carlo code PHITS. The two LET quantities show a very similar behavior for protons with initial energy higher than approximately 17 MeV

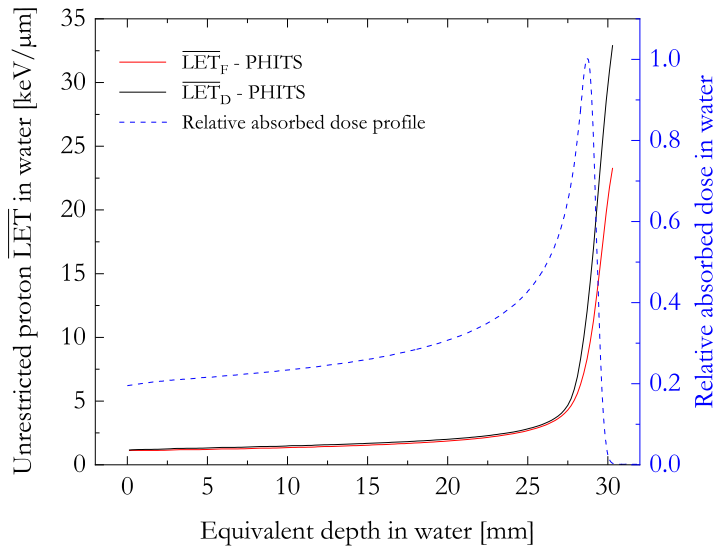

Figure 4. PHITS-simulated fluence-mean ($\overline{\text{LET}}_F$) and dose-mean ($\overline{\text{LET}}_D$) unrestricted proton LET in water as function of the depth in water along the proton Bragg peak.

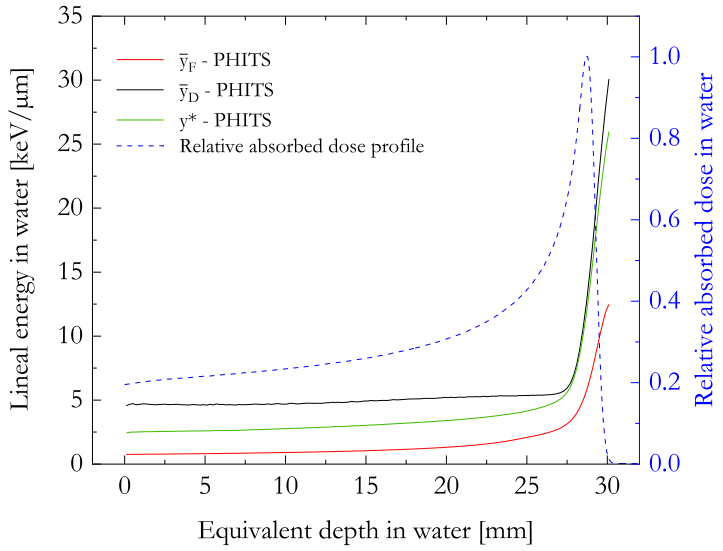

Figure 5. PHITS-simulated frequency-mean ($\bar{y}_F$), dose-mean ($\bar{y}_D$) and saturation corrected ($y*$) lineal energy in water for a 0.564 μm target size as function of the depth in water along the proton Bragg peak.

(^{7}LiF:Mg,Ti/^{7}LiF:Mg,Cu,P dose ratio values smaller than 1.5). At low energies (^{7}LiF:Mg,Ti/^{7}LiF:Mg,Cu,P dose ratio values greater than 2.1), the differences between $\overline{\text{LET}}_F$ and $\overline{\text{LET}}_D$ become more pronounced with the latter quantity being roughly 1.4 times higher than the former one.

3.2.2. *Experimental assessment of the detector ratio*

Figure 7 shows the ratio between the absorbed dose experimentally measured by ^{7}LiF:Mg,Ti (MTS-7) and ^{7}LiF:Mg,Cu,P (MCP-7) detectors as function of the equivalent depth in water along the proton Bragg peak. Here and in the following, the horizontal error bars include both the positioning uncertainty (0.1 mm) and the fact the quantities were averaged over the detector thickness (0.9 mm of lithium fluoride), while the vertical error bars represent the relevant uncertainties of table 1. The experimentally assessed detector ratio was found to range from 1.17 $\pm$ 0.05 at the entrance plateau to 2.2 $\pm$ 0.1 for the last measuring position (equivalent depth in water of the center of the detector = 29.09 mm). The latter values are in agreement with the ones (ratio ranging from 1.12 to 1.90) obtained in a previous measurement campaign during which the detectors were exposed in a clinical proton spread out Bragg peak (SOBP, range ~ 120 mm, modulation ~ 50 mm, max energy ~ 200 MeV) at iThemba LABS (Parisi *et al* 2019a). The small difference in the detector ratio measured at the beam entrance (1.12 at iThemba LABS, 1.17 at IFJ-PAN) is due to higher energy of the proton beam at iThemba LABS (the detector ratio decreases with the increase of the energy). On the other hand, the detector ratio measured at the

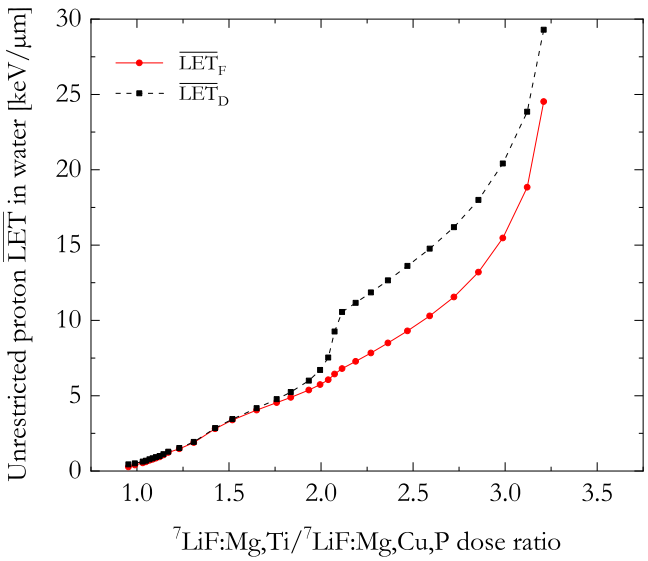

Figure 6. Calibration curves calculated with the Microdosimetric d(z) Model to correlate the unrestricted fluence-mean ($\overline{LET}_F$) and dose-mean ($\overline{LET}_D$) proton LET in water with the expected ratio between absorbed dose measured by ^{7}LiF:Mg,Ti (MTS-7) and ^{7}LiF:Mg,Cu,P (MCP-7) thermoluminescent detectors.

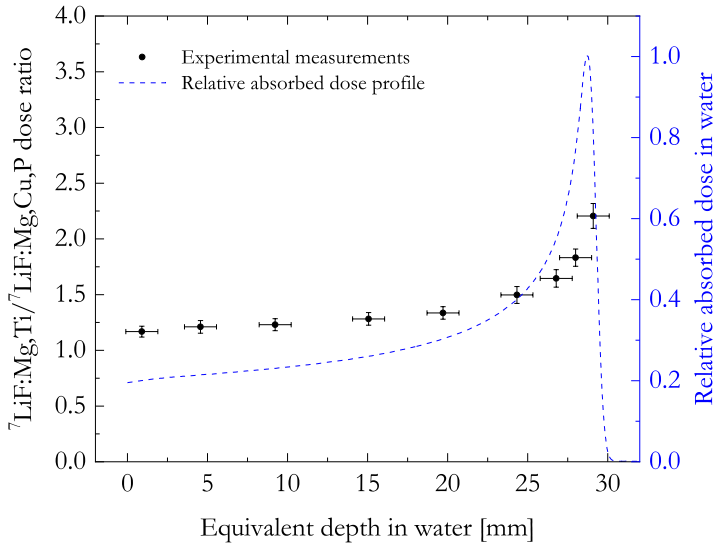

Figure 7. Experimentally assessed ratio between the absorbed doses measured by ^{7}LiF:Mg,Ti (MTS-7) and ^{7}LiF:Mg,Cu,P (MCP-7) thermoluminescent detectors as function of the equivalent depth in water of the center of the detector along the proton Bragg peak. The horizontal error bars represent the water equivalent thickness of the detector and the uncertainty in the positioning.

Table 1. Sources of uncertainty (1σ) considered in this work for the two types of thermoluminescent detectors. The uncertainty in the calibration includes both the statistical spread of the calibration detectors and the repeatability of the process. Because the detector dose ratio methodology is based on the relative response of the two detectors (exposed simultaneously within the proton Bragg peak), the uncertainty (2%) associated with the absorbed dose assessment with the ionization chamber is not included in the calculation of the uncertainty budget related to the assessment of the detector dose ratio.

Uncertainty (1σ)	^{7}LiF:Mg,Ti (MTS-7) detectors [%]	^{7}LiF:Mg,Cu,P (MCP-7) detectors [%]
Statistical spread of the experimental detectors averaged over all positions	0.9	1.5
Calibration with ^{60}Co γ-rays	2.8	2.6
Proton absorbed dose measured with the ionization chamber	2.0	2.0
Combined uncertainty	**3.6**	**3.6**
Conversion from LET in lithium fluoride to LET in water	2.0	
Combined uncertainty in the LET assessment using the detector dose ratio method	**4.7**	

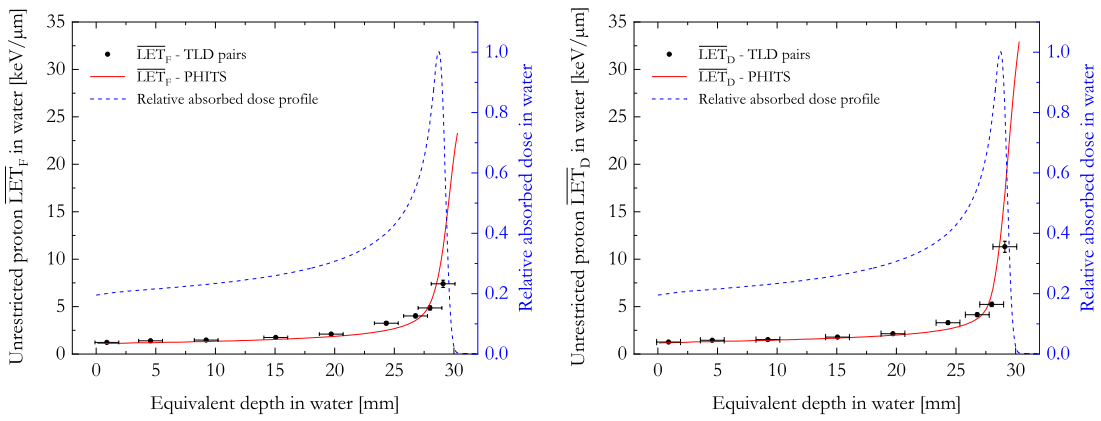

Figure 8. Comparison between the unrestricted fluence- (left) and dose-(right) mean proton LET in water assessed by using the methodology based on the ratio of the absorbed dose values measured by ^{7}LiF:Mg,Ti and ^{7}LiF:Mg,Cu,P detectors ($\overline{LET}$–TLD *pairs*) and the results of radiation transport simulations ($\overline{LET}$–PHITS). The horizontal error bars represent the water equivalent thickness of the detector and the uncertainty in the positioning.

distal edge of the SOBP at iThemba LABS is lower than the one reported in this work. This is due to the longer residual proton range at the last measurement position at iThemba LABS in respect to the one at IFJ-PAN.

3.2.3. Comparison with PHITS-simulated LET values

Using the calibration curves of figure 6 in combination with the experimentally assessed ratio between the absorbed doses measured by ^{7}LiF:Mg,Ti (MTS-7) and ^{7}LiF:Mg,Cu,P (MCP-7) thermoluminescent detectors (figure 7), the unrestricted proton $\overline{LET}_F$ and $\overline{LET}_D$ in water was calculated and compared in figure 8 with the results of the PHITS simulations (figure 4, paragraph 3.1.2 of this paper). As it can be seen, despite the poor spatial resolution of the experimental measurements due to the 1.8 mm water equivalent thickness of the detectors, a good agreement was found for both $\overline{LET}_F$ and $\overline{LET}_D$, with experimental values respectively ranging from 1.23 ± 0.05 keV μm^{-1} and 1.27 ± 0.05 keV μm^{-1} at the entrance plateau to 7.4 ± 0.4 keV μm^{-1} and 11.3 ± 0.6 keV μm^{-1} at the last measuring position.

3.3. Cell death modeling

3.3.1. Linear term of the linear quadratic model

Using the experimentally assessed and PHITS-simulated $\overline{LET}_D$ values as input to the phenomenological model of Carabe *et al* (2012), the α term of the linear quadratic model was calculated using equation (11) as function of the equivalent depth in water in case of HSG cells. Similarly, employing the PHITS-simulated saturation corrected ($y*$) lineal energy in water for a 0.564 μm target size, α was assessed by means of the modified MKM (Kase *et al* 2006) using equation (12) in combination with the optimized MKM parameters of Sato *et al* (2011) for HSG cells. In both cases, the general trend consists in an increase of α with the increase of the equivalent depth in water from a value of approximately 0.29 or 0.25 Gy^{-1} to a maximum of 1.10 or 1.22 Gy^{-1} for the LET-based and the microdosimetric models, respectively. As illustrated in figure 9, most of the changes in the α parameter occurs at depth in water greater than 25 mm. This is due to the fact that both the average LET quantities (figure 4) and the saturation corrected lineal energy (figure 5) were almost invariant for depth in water smaller than the aforementioned value.

A reasonable agreement was found between the results of the LET-based model and the microdosimetric one, with an average relative deviation of 10%. Furthermore, in spite of the poor spatial resolution of the measurements performed with the thermoluminescent detectors, a good agreement is present between the α values predicted using the Carabe *et al* (2012) in combination with the experimentally assessed $\overline{LET}_D$ and the PHITS-simulated one, with all simulated points lying within the uncertainty of the experimental results.

3.3.2. Survival probability

Considering a constant $ß$ and using the previously assessed α values, the survival probability of HSG cells was calculated by means of equation (9) as function of the depth in water. The results are plotted in figure 10 for clinically relevant proton doses at maxima of 2 and 6 Gy. The survival probability was found to decrease with the increase of the depth in water due to the increase of both the absorbed dose and α. In case of a proton dose at maximum of 2 Gy, the survival provability ranges from 0.89 and 0.90 at beam entrance to 0.23 and 0.21 at the Bragg peak for the LET-based and the modified MKM models, respectively. On the other hand, for a proton dose at maximum of 6 Gy, a survival probability at the Bragg peak of 0.002–0.003 was assessed by both methodologies. In this case, the survival probability at beam entrance was determined being 0.66 and 0.69 for the LET-based and the modified MKM models, respectively.

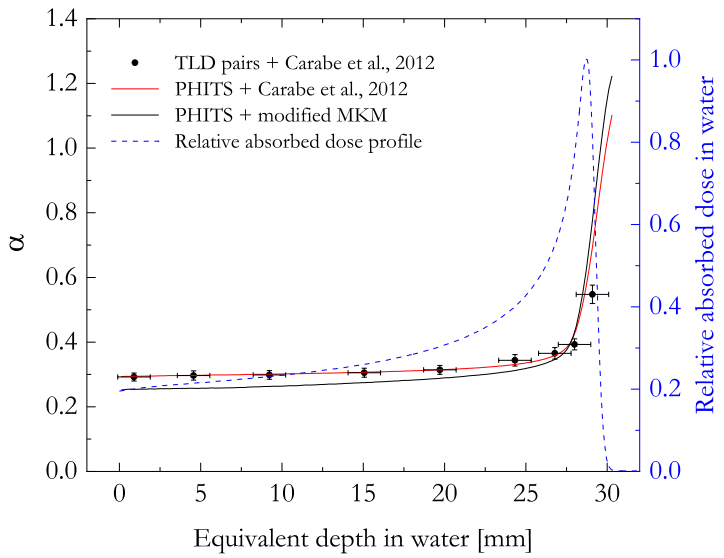

Figure 9. Comparison between the linear term of the linear quadratic model α calculated for HSG cells employing the phenomenological LET-based model of Carabe *et al* (2012) in combination with the experimentally assessed $\overline{\text{LET}}_{\text{D}}$ values using thermoluminescent detectors (TLD pairs + Carabe *et al* 2012) or the PHITS-simulated $\overline{\text{LET}}_{\text{D}}$ values (TLD pairs + Carabe *et al* 2012) and the results of modified MKM of Kase *et al* (2006) in combination with the PHITS-simulated lineal energy probability density (PHITS + modified MKM). The horizontal error bars represent the water equivalent thickness of the detector and the uncertainty in the positioning.

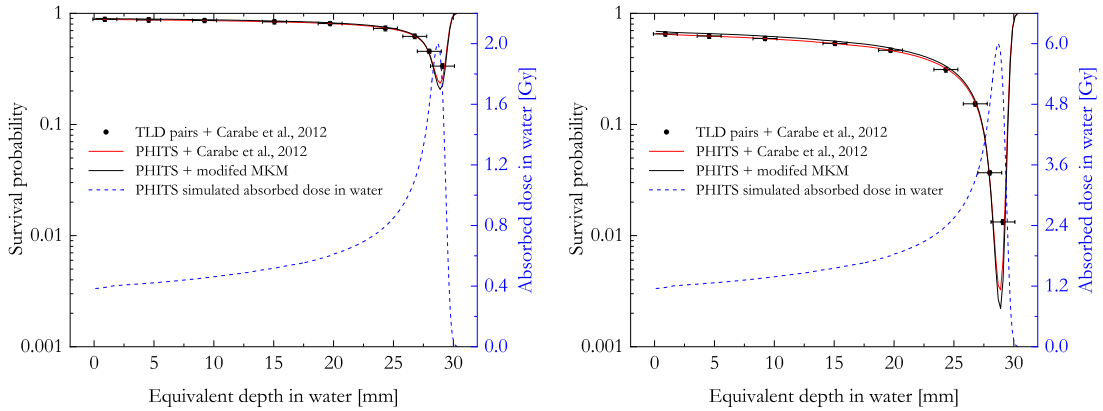

Figure 10. Survival probability of HSG cells as function of the equivalent depth in water as calculated for a proton dose at maximum of 2 Gy (left) and 6 Gy (right) by using the phenomenological LET-based model of Carabe *et al* (2012) in combination with the experimentally assessed $\overline{\text{LET}}_{\text{D}}$ values using thermoluminescent detectors (TLD pairs + Carabe *et al* 2012) or the PHITS-simulated $\overline{\text{LET}}_{\text{D}}$ values (TLD pairs + Carabe *et al* 2012) and the results of modified MKM of Kase *et al* (2006) in combination with the PHITS-simulated lineal energy probability density (PHITS + modified MKM). The horizontal error bars represent the water equivalent thickness of the detector and the uncertainty in the positioning.

The average relative deviation between the results of the two methodologies employing PHITS-simulated physical quantities was 2% and 6% for proton doses at maximum of 2 and 6 Gy, respectively. Additionally, a very good agreement was found also between the results of the ^{7}LiF:Mg,Ti/^{7}LiF:Mg,Cu,P dose ratio methodology in combination with the Carabe *et al* (2012) model and the aforementioned results of PHITS simulations.

3.3.3. *Relative biological effectiveness*

Finally, using equation (10), the RBE was calculated as function of the depth in water for HSG cells in case of proton doses of 2 and 6 Gy. A comparison between the results of the different approaches used in this work can be found in figure 11. The modeling results employing the PHITS-simulated physical quantities show a roughly invariant RBE for depth in water smaller than 25 mm. In this case, the Carabe *et al* (2012) approach indicates a mean RBE value of 0.99 ± 0.02 (proton dose = 2 Gy) and 0.99 ± 0.01 (proton dose = 6 Gy), slightly higher than the 0.93 ± 0.02 (proton dose = 2 Gy) and 0.96 ± 0.02 (proton dose = 6 Gy), assessed by the modified MKM. A sharp RBE increase was observed for positions close to the distal edge, up to maximum values of 2.13 (LET-based model) and 2.27 (modified MKM) for a proton dose of 2 Gy. For a proton dose of 6 Gy, the maximum RBE show lower values, being 1.62 and 1.70 for the LET- and microdosimetry-based models, respectively. The

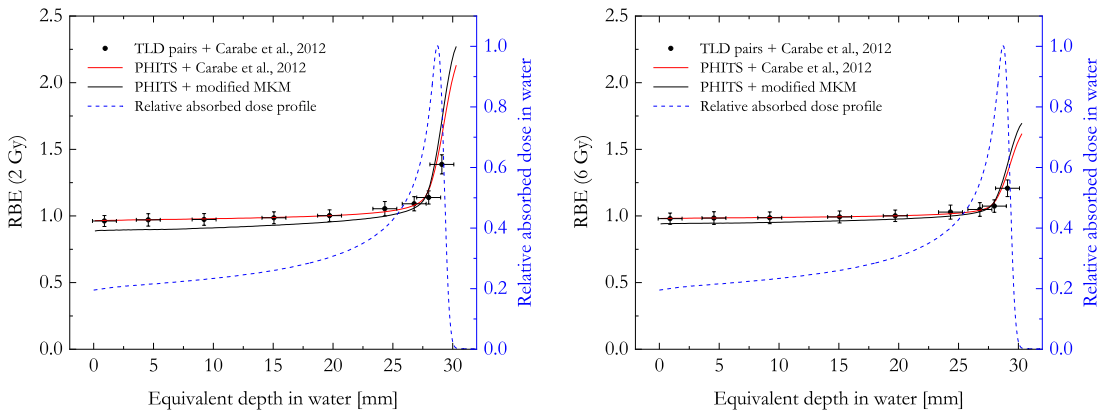

Figure 11. Relative biological effectiveness as function of the equivalent depth in water in case of HSG cells and a proton dose of 2 Gy (left) and 6 Gy (right) as calculated by using the phenomenological LET-based model of Carabe *et al* (2012) in combination with the experimentally assessed $\overline{\text{LET}}_{\text{D}}$ values using thermoluminescent detectors (TLD pairs + Carabe *et al* 2012) or the PHITS-simulated $\overline{\text{LET}}_{\text{D}}$ values (TLD pairs + Carabe *et al* 2012) and the results of modified MKM of Kase *et al* (2006) in combination with the PHITS-simulated lineal energy probability density (PHITS + modified MKM). The horizontal error bars represent the water equivalent thickness of the detector and the uncertainty in the positioning.

average relative deviation between the results of the two aforementioned approaches was 6% and 3% for proton doses of 2 and 6 Gy, respectively. It is worth noticing that the RBE values calculated using the $\overline{\text{LET}}_{\text{D}}$ assessed with the ^{7}LiF:Mg,Ti/^{7}LiF:Mg,Cu,P dose ratio methodology are in agreement with the results making use of PHITS simulations within the experimental uncertainty.

4. Discussion

Three independent, different approaches were employed to assess the RBE changes along the Bragg peak of a clinical proton beam. An experimental approach, based on the measurements with two types of thermoluminescent detectors, was used to derive unrestricted proton dose-mean LET values and calculate the survival fraction and the RBE using the Carabe *et al* (2012) model. Independently, these quantities were also assessed by coupling the aforementioned LET based model (Carabe *et al* 2012) and the modified microdosimetric kinetic model (Kase *et al* 2006) with, respectively, the LET and lineal energy spectra simulated using the Monte Carlo code PHITS. The results were found in very good agreement between each other, with average relative deviations of all the calculated quantities (α term of the linear quadratic model, survival probability for a proton dose of 2 or 6 Gy, RBE for a proton dose of 2 or 6 Gy) ranging from 2% to 10%.

The three methods used for the RBE assessment have complementary nature, both presenting advantages and disadvantages. The technique employing thermoluminescent detectors is based on experimental measurements and might serve as additional, independent verification and quality control of the planned beam delivery and the radiation quality, but it is currently limited by the spatial resolution of the detectors. On the other hand, the computational approaches are characterized by a greater number of obtainable information and a superior spatial resolution, but they might be considered more user, code and lab specific. Additionally, while the microdosimetry method (PHITS + modified MKM) takes into account the creation of secondary particles and their contribution to the microdosimetric spectra for the RBE calculations, the LET based approach takes into account the primary proton beam only. As a consequence, the first could be considered more accurate than its LET-based counterpart. However, this comes at the price of a longer simulation time and a more difficult implementation to clinic.

Furthermore, it is interesting to underline that the assessed RBE values depend strongly on the proton dose under study. For a 2 Gy dose, the RBE for HSG cells ranged from 0.89–0.96 at the entrance plateau to a maximum of 2.13–2.27 at the distal edge. On the other hand, for a proton dose of 6 Gy, the RBE showed a less pronounced increase ranging from 0.94–0.98 to 1.62–1.70. The obtained results were found to be in agreement with the ones reported by Kase *et al* (2013) and Takada *et al* (2017) (RBE values between 0.94 and 1.8) who coupled the modified MKM for HSG cells with the lineal energy distributions respectively measured with a tissue equivalent proportional counter (TEPC) or simulated by PHITS in case of a 155 MeV monoenergetic proton beam. Similarly, microdosimetric distributions measured with the MicroPlus silicon microdosimeter were used to calculate RBE values for HSG cells along the Bragg peak of a 131 MeV proton beam, ranging from 0.96 at the beam entrance to 1.57 the distal falloff (Tran *et al* 2017). As obtained also in the aforementioned studies, the calculated RBE values smaller than 1 at the beam entrance are due the fact that the track structure of energetic protons is characterized by a lower ionization density in respect to the reference radiation which was chosen to be 200 kVp x-rays (Furusawa *et al* 2000). This effect can be quantified by comparing the saturation corrected lineal energy in the both cases. From figure 5 it can be seen that the value of the latter quantity is approximately 3 keV μm^{-1} for positions

close to the beam entrance, while it is approximately 4.2–4.5 keV μm^{-1} in case of 200 kVp x-rays (Coppola *et al* 1976, Okamoto *et al* 2010). If a beam characterized by higher energetic photons was used as reference radiation (i.e. ^{60}Co γ-rays or 6 MV x-rays), the RBE results would have been closer or higher than 1. On the other hand, the Carabe *et al* (2012) model does not explicitly take into account reference radiation's ionization density effects.

The methodology to assess proton $\overline{LET}_F$ and $\overline{LET}_D$ by means of the ratio between the absorbed dose measured by the two detector types (Parisi *et al* 2019a) was improved by including in the calibration curves additional energy points. The average LET quantities assessed as such, were compared with the results of PHITS simulations, showing an agreement within 15%. The calibration curves included in this work were obtained by simulating the energy deposition of monoenergetic protons. This was done aiming to determine generic calibration curves for protons which should not depend on the experimental setup. It was shown in this paper that, considering the experimental uncertainties, this approximation can be judged as acceptable. However, improvements in the calibration curves could be obtained by combining average curves determined in realistic scenarios (pristine and SOBP in water) and it will be the topic of future research.

The above method can find some applications for LET/RBE verification in proton therapy. A need and the consequences of introducing a variable RBE in proton therapy are discussed in literature since more than two decades (Paganetti *et al* 1997, Ödén *et al* 2018). Currently, treatment planning systems (TPSs) for carbon-ion therapy employ phenomenological biophysical models to relate the radiation spectrum (such as for the local effect model, LEM, Elsässer *et al* 2010) or calculated microdosimetric distributions (Inaniwa and Kanematsu 2018) for RBE calculation in the voxel of interest. For therapeutic proton beams, which show lower LET variation, radiobiological models were proposed to relate the RBE to the dose averaged proton $\overline{LET}_D$. Since all major TPS codes for proton therapy include nowadays the option for Monte Carlo transport calculation, this would allow the calculation of $\overline{LET}_D$ and the corresponding RBE for the given dose level. The approach presented in this paper can be applied for in-phantom verification of $\overline{LET}_D$ distributions in a therapeutic plan e.g. by using anthropomorphic phantoms with dedicated spaces for installation of the thermoluminescent detectors, like the Alderson Radiation Therapy Phantom or CIRS Atom phantoms. The other potential application of the proposed approach is to include pairs of LiF:Mg,Ti (MTS) and LiF:Mg,Cu,P (MCP) thermoluminescent detectors for the determination of $\overline{LET}_D$ in mailed dosimetric audits of therapeutic proton beams, allowing an additional cross check for the absorbed dose measurements. In USA the mailed dosimetric audits of proton therapy beams are offered since 2008 by the Imaging and Radiation Oncology Core (Homnick *et al* 2008) but in Europe are still not available. Alanine dosimeters are considered as the most promising detectors for proton beam dose audits due to their perfect dose linearity and the negligible proton energy dependence of their response. Supplementing the audit with the use of LiF:Mg,Ti (MTS)/ LiF:Mg,Cu,P (MCP) pairs will allow also the verification of the beam quality. The spatial and $\overline{LET}_D$ resolution of the method can be further improved by decreasing the diameter and the thickness of both detector types.

5. Conclusions

The paper proved the possibility of using thermoluminescent detectors in combination with biophysical models for assessing LET and RBE quantities in proton therapy beams and to validate the results of Monte Carlo radiation transport simulations. The poor spatial resolution of common thermoluminescent detectors (water equivalent thickness of 1.8 mm) represents the main limitation for their use close to the distal edge of the treatment. However, the latter drawback can be overcome by employing thinner detectors or detectors with a thinner sensitive volume. In both cases, new calibration curves should be evaluated with the Microdosimetric d(z) Model to account for the differences in the detector geometry.

ORCID iDs

Alessio Parisi https://orcid.org/0000-0002-9323-8012
Pawel Olko https://orcid.org/0000-0001-5554-8178
Jan Swakoń https://orcid.org/0000-0001-9262-7326
Tomasz Horwacik https://orcid.org/0000-0003-0521-3876
Hubert Jabłoński https://orcid.org/0000-0002-6712-5540
Leszek Malinowski https://orcid.org/0000-0003-4076-9060
Tomasz Nowak https://orcid.org/0000-0002-5360-1008

References

Bakewicz A, Budzanowski A and Taraszkiewicz R 2003 AIC-144 cyclotron: present status *Nukleonika* **48** S117–21
Belli M, Campa A and Ermolli I 1997 A semi-empirical approach to the evaluation of the relative biological effectiveness of therapeutic proton beams: the methodological framework *Radiat. Res.* **148** 592–8

Bilski P 2002 Lithium fluoride: from LiF: Mg, Ti to LiF: Mg, Cu, P *Radiat. Prot. Dosim.* **100** 199–205
Buchsbaum J C, McDonald M W, Johnstone P A, Hoene T, Mendonca M, Cheng C W, Das I J, McMullen K P and Wolanski M R 2014 Range modulation in proton therapy planning: a simple method for mitigating effects of increased relative biological effectiveness at the end-of-range of clinical proton beams *Radiat. Oncol.* **9** 2
Carabe A, Moteabbed M, Depauw N, Schuemann J and Paganetti H 2012 Range uncertainty in proton therapy due to variable biological effectiveness *Phys. Med. Biol.* **57** 1159
Chaudhary P *et al* 2014 Relative biological effectiveness variation along monoenergetic and modulated Bragg peaks of a 62-MeV therapeutic proton beam: a preclinical assessment *Int. J. Radiat. Oncol. Biol. Phys.* **90** 27–35
Chen Y and Ahmad S 2011 Empirical model estimation of relative biological effectiveness for proton beam therapy *Radiat. Prot. Dosim.* **149** 116–23
Colautti P *et al* 2018 Miniaturized microdosimeters as LET monitors: First comparison of calculated and experimental data performed at the 62 MeV/u ^{12}C beam of INFN-LNS with four different detectors *Phys. Med.* **52** 113–21
Coppola M, Eickel R, Fitzgerald M, Pirrwitz D, Porro F and Booz J 1976 Experimental evaluation of the spectral energy deposition in small volumes by low-LET radiations *Report EUR 5452: Fifth Symposium on Microdosimetry Commission of the European Communities* pp 377–392
Debrot E *et al* 2018 SOI microdosimetry and modified MKM for evaluation of relative biological effectiveness for a passive proton therapy radiation field *Phys. Med. Biol.* **63** 235007–15
Durante M and Paganetti H 2016 Nuclear physics in particle therapy: a review *Rep. Progr. Phys.* **79** 096702
Elsässer T *et al* 2010 Quantification of the relative biological effectiveness for ion beam radiotherapy: direct experimental comparison of proton and carbon ion beams and a novel approach for treatment planning *Int. J. Radiat. Oncol. Biol. Phys.* **78** 1177–83
Frese M C, Wilkens J J, Huber P E, Jensen A D, Oelfke U and Taheri-Kadkhoda Z 2011 Application of constant versus variable relative biological effectiveness in treatment planning of intensity-modulated proton therapy *Int. J. Radiat. Oncol. Biol. Phys.* **79** 80–8
Furusawa Y, Fukutsu K, Aoki M, Itsukaichi H, Eguchi-Kasai K, Ohara H, Yatagai F, Kanai T and Ando K 2000 Inactivation of aerobic and hypoxic cells from three different cell lines by accelerated ^{3}He-, ^{12}C-and ^{20}Ne-ion beams *Radiat. Res.* **154** 485–96
Gieszczyk W and Bilski P 2017 A simplified numerical approach to non-radiation induced high-temperature signals in thermoluminescence. GlowVIEW—a useful tool for a multiple glow-curve analysis *Radiat. Meas.* **107** 102–10
Giovannini G, Böhlen T, Cabal G, Bauer J, Tessonnier T, Frey K, Debus J, Mairani A and Parodi K 2016 Variable RBE in proton therapy: comparison of different model predictions and their influence on clinical-like scenarios *Radiat. Oncol.* **11** 68
Grassberger C and Paganetti H 2011 Elevated LET components in clinical proton beams *Phys. Med. Biol.* **56** 6677
Guan F *et al* 2015 Analysis of the track-and dose-averaged LET and LET spectra in proton therapy using the GEANT4 Monte Carlo code *Med. Phys.* **42** 6234–47
Hawkins R B 1996 A microdosimetric-kinetic model of cell death from exposure to ionizing radiation of any LET, with experimental and clinical applications *Int. J. Radiat. Biol.* **69** 739–55
Hawkins R B 2003 A microdosimetric-kinetic model for the effect of non-Poisson distribution of lethal lesions on the variation of RBE with LET *Radiat. Res.* **160** 61–9
Hirayama H, Namito Y, Nelson W R, Bielajew A F and Wilderman S J 2005 *SLAC Report 730: The EGS5 Code System* Stanford Linear Accelerator Center
Homnick J, Ibbott G, Springer A and Aguirre J 2008 TH-D-352-05: optically stimulated luminescence (OSL) dosimeters can be used for remote dosimetry services *Med. Phys.* **35** 2994–5
Inaniwa T, Furukawa T, Kase Y, Matsufuji N, Toshito T, Matsumoto Y, Furusawa Y and Noda K 2010 Treatment planning for a scanned carbon beam with a modified microdosimetric kinetic model *Phys. Med. Biol.* **55** 6721
Inaniwa T and Kanematsu N 2018 Adaptation of stochastic microdosimetric kinetic model for charged-particle therapy treatment planning *Phys. Med. Biol.* **63** 095011
International Atomic Energy Agency 2000 *TRS-398: Technical Reports Series No. 398: Absorbed Dose Determination in External Beam Radiotherapy, an International Code of Practice for Dosimetry Based on Standards of Absorbed dose to Water* International Atomic Energy Agency, Vienna
International Atomic Energy Agency 2008 Relative biological effectiveness in ion beam therapy *Technical Reports Series* No. 461
International Commission on Radiation Units and Measurements 1983 *ICRU Report 36 Microdosimetry* International Commission on Radiation Units and Measurements, Bethesda
International Commission on Radiation Units and Measurements 2007 *ICRU Report 78 Prescribing, Recording, and Reporting Proton-Beam Therapy*
Jones B 2015 A simpler energy transfer efficiency model to predict relative biological effect for protons and heavier ions *Frontiers Oncol.* **5** 184
Kase Y, Kanai T, Matsumoto Y, Furusawa Y, Okamoto H, Asaba T, Sakama M and Shinoda H 2006 Microdosimetric measurements and estimation of human cell survival for heavy-ion beams *Radiat. Res.* **166** 629–38
Kase Y, Kanai T, Sakama M, Tameshige Y, Himukai T, Nose H and Matsufuji N 2011 Microdosimetric approach to NIRS-defined biological dose measurement for carbon-ion treatment beam *J. Radiat. Res.* **52** 59–68
Kase Y, Yamashita W, Matsufuji N, Takada K, Sakae T, Furusawa Y, Yamashita H and Murayama S 2013 Microdosimetric calculation of relative biological effectiveness for design of therapeutic proton beams *J. Radiat. Res.* **54** 485–93
Loncol T, Cosgrove V, Denis J M, Gueulette J, Mazal A, Menzel H G, Pihet P and Sabattier R 1994 Radiobiological effectiveness of radiation beams with broad LET spectra: microdosimetric analysis using biological weighting functions *Radiat. Prot. Dosim.* **52** 347–52
Lynch G R and Dahl O I 1991 Approximations to multiple Coulomb scattering *Nucl. Instrum. Methods Phys. Res.* B **58** 6–10
Mairani A *et al* 2017 A phenomenological relative biological effectiveness approach for proton therapy based on an improved description of the mixed radiation field *Phys. Med. Biol.* **62** 1378
McKeever S W, Moscovitch M and Townsend P D 1995 *Thermoluminescence Dosimetry Materials: Properties and Uses* (Ashford: Nuclear Technology Publishing)
McMahon S J, Paganetti H and Prise K M 2018 LET-weighted doses effectively reduce biological variability in proton radiotherapy planning *Phys. Med. Biol.* **63** 225009
McMahon S J 2019 The linear quadratic model: usage, interpretation and challenges *Phys. Med. Biol.* **64** 01TR01
McNamara A L, Schuemann J and Paganetti H 2015 A phenomenological relative biological effectiveness (RBE) model for proton therapy based on all published *in vitro* cell survival data *Phys. Med. Biol.* **60** 8399
Moliere G 1948 Theorie der streuung schneller geladener teilchen ii mehrfach-und vielfachstreuung *Zeitschrift für Naturforschung* A **3** 78–97

Ödén J, DeLuca P M and Orton C G 2018 The use of a constant RBE = 1.1 for proton radiotherapy is no longer appropriate *Med. Phys.* **45** 502–5
Okamoto H, Kanai T, Kase Y, Matsumoto Y, Furusawa Y, Fujita Y, Saitoh H, Itami J and Kohno T 2010 Relation between lineal energy distribution and relative biological effectiveness for photon beams according to the microdosimetric kinetic model *J. Radiat. Res.* **52** 1012100177
Ogawa T, Sato T, Hashimoto S and Niita K 2014 Development of a reaction ejectile sampling algorithm to recover kinematic correlations from inclusive cross-section data in Monte-Carlo particle transport simulations *Nucl. Instrum. Methods Phys. Res.* A **763** 575–90
Olko P 2002 Microdosimetric modelling of physical and biological detectors *Habilitation Thesis* Henryk Niewodniczański Institute of Nuclear Physics
Olko P 2004 Microdosimetric modelling of the relative efficiency of thermoluminescent materials *Radiat. Meas.* **38** 781–6
Paganetti H, Olko P, Kobus H, Becker R, Schmitz T, Waligorski M P, Filges D and Müller-Gärtner H W 1997 Calculation of relative biological effectiveness for proton beams using biological weighting functions *Int. J. Radiat. Oncol. Biol. Phys.* **37** 719–29
Paganetti H 2002 Nuclear interactions in proton therapy: dose and relative biological effect distributions originating from primary and secondary particles *Phys. Med. Biol.* **47** 747
Paganetti H, Niemierko A, Ancukiewicz M, Gerweck L E, Goitein M, Loeffler J S and Suit H D 2002 Relative biological effectiveness (RBE) values for proton beam therapy *Int. J. Radiat. Oncol. Biol. Phys.* **53** 407–21
Paganetti H 2014 Relative biological effectiveness (RBE) values for proton beam therapy. Variations as a function of biological endpoint, dose, and linear energy transfer *Phys. Med. Biol.* **59** R419
Paganetti H *et al* 2019 Report of the AAPM TG-256 on the relative biological effectiveness of proton beams in radiation therapy *Med. Phys.* **46** e53–78
Parisi A, Van Hoey O, Mégret P and Vanhavere F 2017a The influence of the dose assessment method on the LET dependence of the relative luminescence efficiency of LiF: Mg, Ti and LiF: Mg, Cu, P *Radiat. Meas.* **98** 34–40
Parisi A, Van Hoey O, Mégret P and Vanhavere F 2017b Deconvolution study on the glow curve structure of LiF: Mg, Ti and LiF: Mg, Cu, P thermoluminescent detectors exposed to ^{1}H, ^{4}He and ^{12}C ion beams *Nucl. Instrum. Methods Phys. Res.* B **407** 222–9
Parisi A, Van Hoey O and Vanhavere F 2017c Microdosimetric modeling of the relative luminescence efficiency of LiF:Mg,Ti (MTS) detectors exposed to charged particles *Radiat. Prot. Dosim.* **180** 1–4
Parisi A, Van Hoey O, Mégret P and Vanhavere F 2017d Microdosimetric modeling of the relative luminescence efficiency of LiF:Mg,Cu,P (MCP) detectors exposed to charged particles *Radiat. Prot. Dosim.* **183** 172–6
Parisi A 2018 Space and hadron therapy dosimetry with luminescent detectors: microdosimetric modeling and experimental measurements *PhD Thesis* Polytech of Mons
Parisi A, de Freitas Nascimento L, Van Hoey O, Mégret P, Kitamura H, Kodaira S and Vanhavere F 2018a Low temperature thermoluminescence anomaly of LiF:Mg,Cu,P radiation detectors exposed to ^{1}H and ^{4}He ions *Radiat. Meas.* **119** 155–65
Parisi A, Van Hoey O, Mégret P and Vanhavere F 2018b Microdosimetric specific energy probability distribution in nanometric targets and its correlation with the efficiency of thermoluminescent detectors exposed to charged particles *Radiat. Meas.* **123** 1–12
Parisi A *et al* 2019a A novel methodology to assess linear energy transfer and relative biological effectiveness in proton therapy using pairs of differently doped thermoluminescent detectors *Phys. Med. Biol.* **64** 085005
Parisi A, Dabin J, Schoonjans W, Van Hoey O, Mégret P and Vanhavere F 2019b Photon energy response of LiF:Mg,Ti and LiF:Mg,Cu,P thermoluminescent detectors: experimental measurements and microdosimetric modeling *Radiat. Phys. Chem.* **163** 67–73
Rosenfeld A B 2016 Novel detectors for silicon based microdosimetry, their concepts and applications *Nucl. Instrum. Methods Phys. Res.* A **809** 156–70
Rørvik E, Thörnqvist S, Stokkevåg C H, Dahle T J, Fjæra L F and Ytre-Hauge K S 2017 A phenomenological biological dose model for proton therapy based on linear energy transfer spectra *Med. Phys.* **44** 2586–94
Rørvik E, Fjæra L F, Dahle T J, Dale J E, Engeseth G M, Stokkevåg C H, Thörnqvist S and Ytre-Hauge K S 2018 Exploration and application of phenomenological RBE models for proton therapy *Phys. Med. Biol.* **63** 185013
Sato T, Watanabe R and Niita K 2006 Development of a calculation method for estimating specific energy distribution in complex radiation fields *Radiat. Prot. Dosim.* **122** 41–5
Sato T, Watanabe R, Kase Y, Tsuruoka C, Suzuki M, Furusawa Y and Niita K 2011 Analysis of cell-survival fractions for heavy-ion irradiations based on microdosimetric kinetic model implemented in the particle and heavy ion transport code system *Radiat. Prot. Dosim.* **143** 491–6
Sato T and Furusawa Y 2012 Cell survival fraction estimation based on the probability densities of domain and cell nucleus specific energies using improved microdosimetric kinetic models *Radiat. Res.* **178** 341–56
Sato T, Watanabe R, Sihver L and Niita K 2012 Applications of the microdosimetric function implemented in the macroscopic particle transport simulation code PHITS *Int. J. Radiat. Biol.* **88** 143–50
Sato T *et al* 2015 Overview of particle and heavy ion transport code system PHITS. In SNA+MC *2013-Joint Int. Conf. on Supercomputing in Nuclear Applications+ Monte Carlo* (EDP Sciences) p 06018
Sato T *et al* 2018 Features of particle and heavy ion transport code system (PHITS) version 3.02 *J. Nucl. Sci. Technol.* **55** 684–90
Swakon J *et al* 2010 Facility for proton radiotherapy of eye cancer at IFJ PAN in Krakow *Radiat. Meas.* **45** 1469–71
Takada K, Sato T, Kumada H, Koketsu J, Takei H, Sakurai H and Sakae T 2017 Validation of the physical and RBE-weighted dose estimator based on PHITS coupled with a microdosimetric kinetic model for proton therapy *J. Radiat. Res.* **59** 91–9
Tilly N, Johansson J, Isacsson U, Medin J, Blomquist E, Grusell E and Glimelius B 2005 The influence of RBE variations in a clinical proton treatment plan for a hypopharynx cancer *Phys. Med. Biol.* **50** 2765
Tran L T *et al* 2017 Characterization of proton pencil beam scanning and passive beam using a high spatial resolution solid-state microdosimeter *Med. Phys.* **44** 6085–95
Unkelbach J, Botas P, Giantsoudi D, Gorissen B L and Paganetti H 2016 Reoptimization of intensity modulated proton therapy plans based on linear energy transfer *Int. J. Radiat. Oncol. Biol. Phys.* **96** 1097–106
Vavilov P V 1957 Ionization losses of high-energy heavy particles *Sov. Phys. JETP* **5** 749–51
Wan Chan Tseung H S, Ma J, Kreofsky C R, Ma D J and Beltran C 2016 Clinically applicable Monte Carlo-based biological dose optimization for the treatment of head and neck cancers with spot-scanning proton therapy *Int. J. Radiat. Oncol. Biol. Phys.* **95** 1535–43
Wedenberg M, Lind B K and Hårdemark B 2013 A model for the relative biological effectiveness of protons: the tissue specific parameter α/β of photons is a predictor for the sensitivity to LET changes *Acta Oncol.* **52** 580–8
Wilkens J J and Oelfke U 2004 A phenomenological model for the relative biological effectiveness in therapeutic proton beams *Phys. Med. Biol.* **49** 2811
Ziegler J F, Ziegler M D and Biersack J P 2010 SRIM—the stopping and range of ions in matter (2010) *Nucl. Instrum. Methods Phys. Res.* B **268** 1818–23